HHS Public Access

Author manuscript

J Nonnewton Fluid Mech. Author manuscript; available in PMC 2016 November 01.

Published in final edited form as:

J Nonnewton Fluid Mech. 2015 November ; 225: 62–69. doi:10.1016/j.jnnfm.2015.09.002.

Contact Line Instability of Gravity-Driven Flow of Power-Law Fluids

Bin Hu and **Sarah L. Kieweg***

Department of Mechanical Engineering, University of Kansas, Lawrence, KS 66045

Abstract

The moving contact line of a thin fluid film can often corrugate into fingers, which is also known as a fingering instability. Although the fingering instability of Newtonian fluids has been studied extensively, there are few studies published on contact line fingering instability of non-Newtonian fluids. In particular, it is still unknown how shear-thinning rheological properties can affect the formation, growth, and shape of a contact line instability. Our previous study (Hu and Kieweg, 2012) showed a decreased capillary ridge formation for more shear-thinning fluids in a 2D model (i.e. 1D thin film spreading within the scope of lubrication theory). Those results motivated this study's hypothesis: more shear-thinning fluids should have suppressed finger growth and longer finger wavelength, and this should be evident in linear stability analysis (LSA) and 3D (i.e. 2D spreading) numerical simulations. In this study, we developed a LSA model for the gravity-driven flow of shear-thinning films, and carried out a parametric study to investigate the impact of shear-thinning on the growth rate of the emerging fingering pattern. A fully 3D model was also developed to compare and verify the LSA results using single perturbations, and to explore the result of multiple-mode, randomly imposed perturbations. Both the LSA and 3D numerical results confirmed that the contact line fingers grow faster for Newtonian fluids than the shear-thinning fluids on both vertical and inclined planes. In addition, both the LSA and 3D model indicated that the Newtonian fluids form fingers with shorter wavelengths than the shear-thinning fluids when the plane is inclined; no difference in the most unstable (i.e. emerging) wavelength was observed at vertical. This study also showed that the distance between emerging fingers was smaller on a vertical plane than on a less-inclined plane for shear-thinning fluids, as previously shown for Newtonian fluids. For the first time for shear-thinning fluids, these results connect trends in capillary ridge and contact line finger formation in 2D models, LSA, and 3D simulations. The results can provide us insights on how to optimize non-Newtonian fluid properties to minimize a fingering instability in many industrial and biological applications.

Graphical Abstract

*Corresponding author. Address: 1530 W. 15th St., 3138 Learned Hall, Lawrence, KS 66045.United States. Tel.: +1 7858644575; fax: +1 7858645254. kieweg@ku.edu (S.L. Kieweg)..

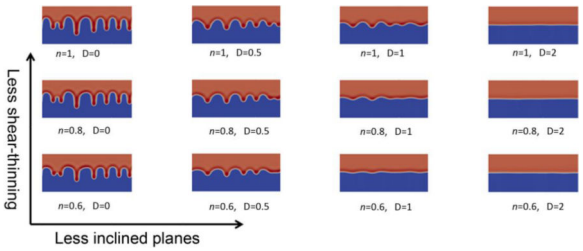

Keywords

Thin film flow; Fingering instability; Linear stability analysis; Non-Newtonian fluids; Shear-thinning effect; 3D simulation

1. Introduction

Gravity-driven thin film flow with fingering instability is of interest in many fields, such as industry (paints [1], contact lens manufacture [2], and microchip fabrication [3]), nature (lava flow [4] and glacier flow [5]), and biomedical applications (microbicidal drug delivery [6, 7], eye tears and substitutes [8]). In many of the applications, a uniform coating is desired with no dry spots. Thus, it is very important to understand the mechanics of the fingering instability at the moving contact line of a spreading thin film.

Numerous experimental and analytical/numerical studies have examined the dynamics of a gravity-driven contact line following the famous study of Huppert [9]. Schwartz [10] proved the contact line instability is controlled by surface tension effects. Troian et al. [11] carried out linear stability analyses (LSA) on thin film flow and derived the formulation under the limit of small wavenumber to show the capillary ridge was responsible for the instability. Bertozzi and Brenner [12] verified the LSA numerically and developed the transient model to investigate the transient growth of the fingering instability. Lin and Kondic [13] studied the instability of the thin film flowing down an inverted incline. These studies all assumed a constant flux configuration, however, in practical applications, constant-volume configuration is often needed. In our previous 2D study [6], we showed how the capillary ridge at the front of the flow evolves for a constant volume configuration. Espin and Kumar developed a 2D constant-volume model to study the thin film flow of colloidal suspensions, and showed both the particle concentration and the evaporation have a large impact on the front interface [14, 15]. Gonzalez and Gomba developed a predictive model and integral method to study the linear stability of the constant volume flow [16, 17]. All these studies provide a systematic approach to deal with the capillary ridge and contact line instability problem.

However, most of those previous studies were for Newtonian fluids. The fluids used in the above mentioned industrial and biomedical applications usually exhibit non-Newtonian behavior, especially shear-thinning behavior. There are few published studies on contact line instability of non-Newtonian fluids. Balmforth *et al.* [18] studied the instability of Bingham fluids using LSA and showed the yield stress stabilized the contact line. Spaid and Homsy [19, 20] used energy analysis for viscoelastic fluids to show elasticity has a stabilizing effect

on the capillary ridge. It is still unknown how the shear-thinning behavior, for non-Newtonian fluids can affect the contact line instability. In our previous work [6], we completed a 2D analysis of shear-thinning fluids. Using travelling waves and numerical simulations of one-dimensional spreading, we found that increasing the shear-thinning behavior of polymer solutions decreased the capillary ridge height. This leads to the hypothesis for this study: that more shear-thinning fluids should have suppressed finger growth and longer finger wavelength, and that this should be evident in linear stability analysis and 3D numerical simulations. In summary, the relationship between the emergence and height of a capillary ridge in a 2D shear-thinning model has not previously been related to the linear stability analysis and 3D numerical model of the contact line instability. To solve this issue, we need to develop a contact line model of power-law fluids and identify the importance of different factors affecting fingering instability.

To verify the linear stability analysis for a Newtonian fluid, Kondic and Diez [21-25] numerically studied the 3D flow to simulate the fingering instability in the transverse direction. Lin et al. [26] studied 3D simulations for fluids on an inverted incline for unevenly distributed fluid viscosity. Those studies were also only for Newtonian fluids. Our research group has developed a 3D model for power-law fluids [27] and Ellis fluids [28] to study the spreading speed of a polymer solution and compare to experiments. However, those models did not incorporate the surface tension effect, and therefore cannot simulate the fingering instability.

The goals of this study were to: (a) in Section 2, develop a contact line model using LSA, and study how the shear-thinning effect would influence the finger growth, and (b) in Section 3, expand to 3D flow simulations with various perturbations to verify the LSA results.

2. Linear stability analysis

2.1 Methods for linear stability analysis

The fluid is described by power-law constitutive model:

$$\tau_{ij}=m|II_{2D}|^{\frac{n-1}{2}}(2D_{ij})\,[29]$$

where $\tilde{\tilde{\tau}}$ is the stress tensor, m is the consistency of power-law fluid, $2\tilde{\tilde{D}}=(\nabla\tilde{v})^T+\nabla\tilde{v}$ is the shear rate tensor, $\tilde{v}$ is the velocity vector, and $II_{2D}=(1/2)\left[\left(tr2\tilde{\tilde{D}}\right)^2-tr\left(2\tilde{\tilde{D}}\right)^2\right]$ is the second invariant of the shear rate tensor.

To describe the movement of the fluid's free surface flow down an incline, a wetting flow assumption and thin film lubrication approximation are commonly used. A non-dimensional partial differential equation (PDE) for the 3D flow (i.e. 2D spreading) of power-law fluids can be obtained for the height of the fluid as a function of space and time, $h(x,y,t)$. A similar detailed derivation was shown in Perazzo et al. [30] and our previous publications on power-

law models [6, 27]. The resulting non-dimensional thin film equation for a power-law fluid is:

$$\frac{\partial h}{\partial t}+\frac{\partial}{\partial x}\left\{h^{\frac{1}{n}+2}\left\{\left[1-D\frac{\partial h}{\partial x}+\frac{\partial(\Delta h)}{\partial x}\right]^2+\left[D\frac{\partial h}{\partial y}-\frac{\partial(\Delta h)}{\partial y}\right]^2\right\}^{\frac{1}{2n}-\frac{1}{2}}\left[1-D\frac{\partial h}{\partial x}+\frac{\partial(\Delta h)}{\partial x}\right]\right\} -\frac{\partial}{\partial y}\left\{h^{\frac{1}{n}+2}\left\{\left[1-D\frac{\partial h}{\partial x}+\frac{\partial(\Delta h)}{\partial x}\right]^2+\left[D\frac{\partial h}{\partial y}-\frac{\partial(\Delta h)}{\partial y}\right]^2\right\}^{\frac{1}{2n}-\frac{1}{2}}\left[D\frac{\partial h}{\partial y}-\frac{\partial(\Delta h)}{\partial y}\right]\right\}=0 \quad (1)$$

where n is the power-law index and $n < 1$ indicates shear-thinning fluids. The dimensionless parameter $D = cot\alpha(Ca)^{1/3}$ reflects the magnitude of the normal component of gravity force (e.g. $D = 0$ is vertical, $D = 1$ is inclined). The dimensionless parameter $Ca = \mu_0 U/\gamma$ is the power-law capillary number, α is the inclination angle, and γ is the surface tension coefficient. U is a characteristic velocity and μ_0 is a characteristic viscosity incorporating the power-law terms. These latter terms follow the dimensionless groups used for Newtonian fluids [12, 21], and were further modified for the power-law variation as described in more detail in Appendix D of our previous study [6].

To conduct a linear stability analysis (LSA), we first determine a traveling wave solution. The method described here for traveling waves and LSA follows the general approach described in detail for Newtonian fluids by previous authors, e.g. in [12, 21]. To find a traveling wave solution, we assume $h(x, y, t)$ is y-independent to reduce Eq. 1 to its 2D form. Then, we assume constant flux boundary conditions such that the fluid height is flat far from the moving front: $x \to -\infty$, $h \to 1$ and $x \to \infty$, $h \to b$, where $b << 1$ is the thickness of the precursor. This boundary condition leads to a traveling wave solution $h_0(x, t)$ in the x direction. Using a moving reference frame, $x^* = x - Ut$ traveling with velocity U, the following ODE for $h_0(x^*, t)$ is obtained (dropping * from here forward)

$$-Uh_0+\left\{h_0^{\frac{1}{n}+2}\left\{\left[1-D(h_0)_x+(h_0)_{xxx}\right]^2\right\}^{\frac{1}{2n}-\frac{1}{2}}\left[1-D(h_0)_x+(h_0)_{xxx}\right]\right\}=f \quad (2)$$

where the boundary conditions also result in the following expressions

$$U=\frac{1-b^{\frac{1}{n}+2}}{1=b}, \quad f=\frac{-b+b^{\frac{1}{n}+2}}{1-b}$$

Eq. 2 was numerically solved (see Appendix C of [6]) for the traveling wave solution, which may form a capillary ridge. The presence and height of the ridge depends on many factors, such as D and the power-law index, n [6].

Next, we can use this traveling wave solution as the 'base' solution in the x direction. When we try to expand to the transverse y direction, we can simply assume the solution is in the form of a base state h_0 with a perturbation h_1, $h(x, y, t) = h_0(x) + \in h_1(x, y, y)$, where h_0 , h_1 are of $O(1)$ and $\in << 1$, and substitute it into the thin film PDE (Eq 1). Only terms that are on the order of $\in$ are kept in the resulting equation, and h_1 can be expressed as a Fourier transform using the superposition principle, $h_1(x, y, t) = \int_{-\infty}^{0} g(x,t)\, e^{iqy} dq$, where q is the

wavenumber. We apply the Taylor series to expand the power terms in Eq. 1. The Taylor approximation is kept in the same order of $\in$. We also use the traveling wave solution of Eq. 2 to substitute the higher order terms. After simplification, we can obtain a PDE for $g(x, t)$:

$$\frac{\partial g}{\partial t}+\frac{\partial}{\partial x}\left\{\left\{\left[\frac{(Uh_0+f)}{h_0^{\frac{1}{n}+2}}\right]^{2n}\right\}^{\frac{1}{2n}-\frac{1}{2}}\left\{\left(\frac{1}{n}+2\right)h_0^{\frac{1}{n}+1}\left\{\left[\frac{(Uh_0+f)}{h_0^{\frac{1}{n}+2}}\right]^{2}\right\}^{\frac{n}{2}-\frac{1}{2}}\left[\frac{(Uh_0+f)}{h_0^{\frac{1}{n}+2}}\right]g+\frac{1}{n}h_0^{\frac{1}{n}+2}\left[\left(-q^2-D\right)g_x+g_{xxx}\right]\right\}\right\}$$
$$-\left\{\left[\frac{(Uh_0+f)}{h_0^{\frac{1}{n}+2}}\right]^{2n}\right\}^{\frac{1}{2n}-\frac{1}{2}}h_0^{\frac{1}{n}+2}\left[q^2\left(-Dg-q^2g+g_{xx}\right)\right] \quad (3)$$
$$-U\frac{\partial g}{\partial x}=0$$

The solution of Eq. 3 provides information about the growth of an imposed perturbation, and how that growth depends on the wavenumber. The growth rate, σ, of $g(x, t)$ is defined from the exponential time dependence of $g = \phi(x)e^{\sigma t}$ due to the homogeneity of Eq. 3, and that growth rate will be a function of the wavenumber. In the following sections, we will solve this PDE using both analytical analysis and numerical methods.

2.1.1 Small wavenumber analysis—To obtain an analytical solution of Eq. 3 for *g(x,t)* we follow the approach in [11, 21], summarized as follows. We first need to assume that the wavenumber q is small, so we can write

$$g=g_0+q^2g_1 \quad (4)$$

and the growth rate is thus

$$\sigma=q^2\sigma_1 \quad (5)$$

We substitute Eq. 4 and Eq. 5 into Eq. 3, and the second order, $O(q^2)$, terms give

$$\sigma_1\varphi_0+\frac{\partial}{\partial x}\left(\left\{\left[\frac{(Uh_0+f)}{h_0^{\frac{1}{n}+2}}\right]^{2n}\right\}^{\frac{1}{2n}-\frac{1}{2}}\left\{\left(\frac{1}{n}+2\right)h_0^{\frac{1}{h}+1}\left\{\left[\frac{(Uh_0+f)}{h_0^{\frac{1}{n}+2}}\right]^{2}\right\}^{\frac{n}{2}-\frac{1}{2}}\left[\frac{(Uh_0+f)}{h_0^{\frac{1}{n}+2}}\right]\varphi_1+\frac{1}{n}h_0^{\frac{1}{n}+2}\left[-\varphi_{0,x}-D\varphi_{1,x}+\varphi_{1,xx}\right.\right.\right.$$
$$\left.-\left\{\left[\frac{(Uh_0+f)}{h_0^{\frac{1}{n}+2}}\right]^{2n}\right\}^{\frac{1}{2n}-\frac{1}{2}}h_0^{\frac{1}{n}+2}\left[(-D\varphi_0+\varphi_{0,xx})\right]-U\varphi_{1,x}=0 \quad (6)$$

We can integrate Eq. 6 over the domain in x $[-\infty, 0]$, and substitute ϕ_0 for $h_{0,x}$. After applying the traveling wave solution and $\phi_1 \to 0$ at the boundary conditions, we can obtain the growth rate as a function of a base solution, h_0:

$$\sigma_1=\int_{-\infty}^{0}h_0\left(h_0^{1+n}-1\right)dx \quad (7)$$

Note, we assume precursor $b = 0$ to further simplify the problem, and directly compare to the result for Newtonian fluids in [21].

Eq. 7 is used in this small wavenumber analysis to show why the capillary ridge examined in our previous 2D study [6] is important. When the base solution has a capillary ridge (i.e. $h_0(x) > 1$), Eq. 7 indicates that the growth rate is positive, and thus the contact line is unstable. If the growth rate is negative, the perturbation does not grow, and the fingering instability is suppressed. This conclusion from Eq. 7 for our shear-thinning fluids is consistent with the studies for Newtonian fluids [11, 21]. The conclusion of this analytical solution for small wavenumbers connects this LSA analysis to our previous 2D model [6], where we investigated how the capillary ridge is affected by the shear-thinning effect and D, which in turn impact the base solution and thus growth rates. To completely and further examine the impact of these terms on the growth rate, we numerically solved for all wavenumbers as described in the next section.

2.1.2 Numerical approach—Following the procedure outlined by Kondic [21] for Newtonian fluids, the PDE for $g(x,t)$ (Eq. 3) for arbitrary perturbation wavenumbers can be numerically solved with the following steps:

1. Obtain the traveling wave base solution, $h_0(x)$, using numerical methods for a constant-flux condition (as in our previous 2D power-law study [6]).
2. For a given wavenumber q and known base solution, $h_0(x)$, the PDE for $g(x, t)$ (Eq. 3) can be solved numerically. We developed a C code to solve the PDE (Eq. 3) using an implicit finite difference scheme. We applied the Crank–Nicolson method for the time derivative and central difference for the space derivatives. Newton's method was used to solve the algebraic equations resulting from finite difference discretization.
3. Once $g(x, t)$ is obtained, the growth rate σ as a function of wavenumber can be calculated by assuming $g(x, t)$ depends exponentially on time using:

$$\sigma = \frac{1}{g}\frac{\partial g}{\partial t}$$

4. Solve for other q for all modes by repeating 2-3, and plot growth rate σ as a function of wavenumber q.

2.2 Results and discussion: LSA

Figure 1 shows the LSA results for Newtonian ($n = 1$) and shear-thinning fluids ($n = 0.6$, 0.8). If the growth rate is positive, it indicates the contact line is not stable. We can see the growth rate is bigger on the vertical plane ($D = 0$) than the less-inclined planes ($D = 0.5$ and 1) for all three fluids. Also, the growth rates are larger for Newtonian fluids than shear-thinning fluids. For $D = 2$, the growth rate is never positive, indicating the fingering instability is suppressed. The Newtonian results agreed with the existing studies in literature [12, 21]. It is interesting to see the most unstable wavenumbers for all three types of fluids on the vertical plane ($D = 0$) are the same, while for the flatter planes ($D = 0.5$ and 1), the most unstable wavenumbers for shear-thinning fluids are smaller than the Newtonian fluid. We will further discuss this in section 3, in conjunction with the 3D results.

The impact of the precursor thickness on fingering instability has been investigated in previous studies for Newtonian fluids. Both numerical [12, 17] and experimental [31] studies have indicated that increasing the thickness of the precursor can suppress the fingering instability of Newtonian fluids. The growth rate curves of a shear-thinning fluid (n = 0.8) shown in Figure 2 indicate the same trend holds for the power-law fluid. As the precursor thickness increases, the growth rate is decreased.

In our previous 2D study [6], we found the capillary ridge height increases with increasing power-law index n, but decreases with increasing precursor thickness b. Those conclusions match these LSA results very well. This numerically shows the capillary ridge is directly related to the contact line fingering instability, which is consistent with the analytical analysis in 2.1.1.

3. 3D simulations

To further study the fingering instability, we decided to expand to the third, transverse direction and numerically solve the 3D thin film PDE (Eq 1). Finite Element Method (FEM) was used for this part of study. A finite element solver, Dolfin [32] was used for automated assembly of the variational forms of the thin film equation (Eq 1) over the computational domain. Some other libraries used in this study along with Dolfin are components of the open source FEniCS Project [33].

3.1 Finite element formulation

The weak form of equations can be derived from Eq. 1 as follows:

$$\int qhd\Omega - \int qh' d\Omega + \Delta t \int q\left[\frac{\partial}{\partial x}(T) - \frac{\partial}{\partial y}(K)\right] d\Omega - \int U\frac{\partial h}{\partial x} d\Omega = 0$$

$$\int vTd\Omega - \int vh^{\frac{1}{n}+2}\left\{\left[1 - D\frac{\partial h}{\partial x} + \frac{\partial C}{\partial x}\right]^2 + \left[D\frac{\partial h}{\partial y} - \frac{\partial C}{\partial y}\right]^2\right\}^{\frac{1}{2n}-\frac{1}{2}}\left[1 - D\frac{\partial h}{\partial x} + \frac{\partial C}{\partial x}\right] d\Omega = 0$$

$$\int pKd\Omega - \int ph^{\frac{1}{n}+2}\left\{\left[1 - D\frac{\partial h}{\partial x} + \frac{\partial C}{\partial x}\right]^2 + \left[D\frac{\partial h}{\partial y} - \frac{\partial C}{\partial y}\right]^2\right\}^{\frac{1}{2n}-\frac{1}{2}}\left[D\frac{\partial h}{\partial y} - \frac{\partial C}{\partial y}\right] d\Omega = 0$$

$$\int oCd\Omega + \int \nabla o \cdot \nabla h d\Omega = 0$$

where q, v, p and o are test functions, and h' is from the previous time step.

3.2 Numerical parameters

As shown in Figure 3, we suppose the flow is from left to right along the x direction. The boundary conditions in the flow direction are implemented as:

$$h(0, y, t) = 1, \quad h_x(0, y, t) = 0$$
$$h(L_x, y, t) = b, \quad h_x(L_x, y, t) = 0$$

where L_x is the dimensionless length of the computational domain. In the lateral y direction, a periodic boundary condition is specified at $y = 0$ and $y = L_y$:

$$h(x, 0, t) = h(x, L_y, t)$$

For the initial condition, we used a step function similar to our 2D [6] and LSA studies (see Section 2): $h = 1$ at $x = [0, \frac{L_x}{2}]$, and $h = b$ at $x = [\frac{L_x}{2}, L_x]$. To ease the simulation, the step function for the initial profile is smoothed as follows:

$$h(x, y, 0) = Max\left(\frac{1}{1+exp\left(-4\left(x-\frac{L_x}{2}\right)\right)}, b\right)$$

To impose the perturbation at the contact line, we substitute $x = x_0 - 0.2cos(2\pi y/\lambda)$ into the above equation, so the contact line is convex slightly into the flow direction, where λ is the single mode wavelength of the perturbation. The width of the computational domain for single mode simulations is set to the specified wavelength of the simulation. To simulate randomly imposed perturbations, we used a 50-mode sinusoidal function to perturb the contact line:

$$x = x_0 - \sum_{i=1}^{50} A_i cos\left(2\pi y/\lambda_i\right)$$

characterized by $\lambda_i = 2L_y/i$, where $i = 1,2, \ldots 50$ and $L_y = 96$. The amplitudes A_i of the sinusoidal functions are random numbers from [−0.2, 0.2].

All 3D simulations were performed on a Lagrange linear polynomial space with continuous Galerkin method, with element size of $\Delta x = \Delta y = 0.2$. For the time space, we used Crank–Nicolson method with $\Delta t = 0.01$. Both the spatial mesh size and the time step were determined through convergence studies and consideration of computational runtime.

3.3 Results and Discussion: 3D simulations

3.3.1 Comparison with LSA—In this section, we test three perturbation wavelengths on both a Newtonian fluid ($n = 1$) and shear-thinning fluid ($n = 0.6$) to compare with the LSA results presented in Section 2. Both the vertical plane case ($D = 0$) and less-inclined plane case ($D = 1$) are investigated in this section. Note, we use a single mode perturbation by making the single wavelength equal to the domain length L_y in the y direction: $\lambda = L_y$.

***D* = 0 Case:** We first show the simulation results for the vertical plane. Three wavelengths of perturbations are chosen for this series of simulations and are indicated with vertical lines in the LSA results for $D = 0$ (Figure 1a): $\lambda = 4\pi$, 8.7, and 2π. These were selected because the growth rates for the Newtonian fluid ($n = 1$) and shear-thinning fluid ($n = 0.6$) are either both positive at $\lambda = 4\pi$ or both negative at $\lambda = 2\pi$. The $\lambda = 8.7$ was selected because the Newtonian fluid has the positive growth rate, whereas the shear-thinning fluid's growth rate approaches zero.

Figure 4 demonstrates the results of the 3D simulations over time with $\lambda = 4\pi$, 8.7, and 2π wavelength. For the top three cases (both Newtonian and shear-thinning fluids cases at $\lambda = 4\pi$, Newtonian fluid case at $\lambda = 8.7$), the perturbed contact line evolved into a growing finger. This matches the LSA result in Figure 1a, which indicates growth rates for these

three cases are greater than zero. The simulations in Figure 4 also show that the perturbations of the Newtonian fluid (n = 1) grows faster than shear-thinning fluid (n = 0.6) for $\lambda = 4\pi$ and λ = 8.7. Again, those trends match the LSA results (Figure 1a) showing the growth rate is bigger for Newtonian fluids at these wavelengths. As expected from the negative growth rate for $\lambda = 2\pi$ LSA results, the perturbations in the bottom two rows of Figure 4 are suppressed.

D=1 Case: Similar trends and comparisons to LSA can be found on a less-inclined plane (D = 1). The LSA results in Figure 1c indicate vertical lines at three wavenumbers selected for analysis here. The corresponding three wavelengths were: $\lambda = 8\pi$ 18, and 4π. The growth rate for the Newtonian fluid (n = 1) and the shear-thinning fluid (n = 0.6) are either both positive at $\lambda = 8\pi$ or both negative at $\lambda = 4\pi$. At λ = 18, only a Newtonian fluid has the positive growth rate, whereas the most shear-thinning fluid's growth rate approaches zero. The 3D simulations for these three single wavelength perturbations are shown in Figure 5. The simulations demonstrate that for cases with positive growth rates in the LSA results (Figure 1c), all contact lines evolve into fingers (top three rows in Figure 5). For those cases with zero or negative growth rate in the LSA results, the contact lines remain unchanged or become flat. In addition, as seen in the vertical case (D = 0, Figure 4), the contact line of the Newtonian fluid at D = 1 is more unstable than the shear-thinning fluid.

However, there is an important difference between the vertical and less-inclined cases. From the LSA results in Fig 1, we notice that the corresponding wavelength of the largest growth rate for the vertical case ($\lambda = 4\pi$ for Newtonian) is much smaller than the most unstable wavelength for the less-inclined case (e.g. λ = 18 for Newtonian). This trend agrees with published laboratory experiments for Newtonian fluids [21]: the distance between emerging fingers were smaller on a vertical plane than on a less-inclined plane. That trend also occurred for shear-thinning fluids: the most unstable wavelength for the vertical case ($\lambda = 4\pi$ for shear-thinning) is much smaller than the one for the less-inclined case (e.g. $\lambda = 8\pi$ for n = 0.6 shear-thinning). The LSA results also show that the most unstable wavelength increases for more shear-thinning fluids, but that is only observed at smaller inclinations. In Section 3.3.2 below, we look for the same trends using 3D simulations with multiple mode perturbations, to better simulate a physical experiment.

To further compare growth rates, Figure 6 quantitatively compares the growth rate of a finger from 3D simulations and the growth rate of a perturbation from LSA results. The finger length, L, in the simulation is measured from tip to root and is normalized by the initial finger length L_0 from the imposed initial condition. We can see for early times, the growth rate of the finger length from the 3D simulation matches very well with the LSA results. But at later times in the 3D simulation, the finger growth slows and approaches a slower constant speed. This behavior is because at longer times, only a small domain at the front is affected by the surface tension. Thus, the overall traveling speed is therefore decided by the traveling wave speed from the constant flux condition. This speed can be calculated using the similarity solution [6]. Similar results for Newtonian fluids can be found in the experimental study in [21], where comparison is made between experimental data and LSA.

3.3.2 Simulation of multiple mode, randomly imposed perturbations—In addition to the single mode perturbation, it's also interesting to look at how the contact line is affected by multiple-mode, randomly imposed perturbations. Figure 7 shows the $D = 0$ vertical case as an example to demonstrate how the initial perturbed contact line evolves into finger-like rivulets over time a for Newtonian fluid (Figure 7a, $n = 1$) and a shear-thinning fluid (Figure 7b, $n = 0.6$). The randomly perturbed contact line will corrugate into fingering patterns with similar distances between each finger, for a given simulation. The exceptions are the areas where two fingers with similar wavelength merge to form an 'abnormal' wider finger. This can also be observed in our laboratory experiments. An interesting finding is that the merging of the two fingers occurs earlier for the shear-thinning fluid ($n = 0.6$) in Figure 7b than Newtonian fluid ($n = 1$) in Figure 7a. Although the two fingers in the Newtonian case emerge at earlier times (not shown), they grow faster and stay independent for longer compared to the shear-thinning fingers, and this makes them more resistant to merging.

The typical distance between the fingering patterns is related to the most unstable wavenumber in LSA results, according to the existing literature for Newtonian fluids [21, 26]. To check this for shear-thinning fluids, we can use the two $D = 0$ cases in Figure 7 to compare with the LSA results. According to Figure 6, LSA results are accurate at early times. Therefore, for the $D = 0$ cases, we chose $t = 60$ for the comparison. From Figure 7 at $t = 60$, there are seven fingers (prior to merging) across the width (of 96) at the contact line for both the Newtonian and shear-thinning cases. Therefore the average wavelength is approximately $96/7 \approx 13.7$. That is about 9% different from the most unstable wavelength (4π) for both $n = 1$ and $n = 0.6$, found from the $D = 0$ LSA results shown in Figure 1a.

Similar results can be found for the other 3D simulation cases of D and n, and are summarized in Figure 8 and Table 1. Figure 8 compares 3D simulations at one time point for all values of D and n. The times chosen for the contact line patterns in Figure 8 are based on the growth rate results shown in Figure 6 such that a time point is selected in the range when LSA corresponds to the 3D simulation. Similar to the $D = 0$ case, the average wavelength calculated from 3D simulations match the most unstable wavelength from LSA results quantitatively. However, unlike the $D = 0$ case, where the average distance between fingers are the same for the three types of fluids, the finger wavelength can vary as a function of shear-thinning for the less-inclined cases. For less-inclined simulations ($D = 0.5$ and 1), the $n = 1$ and 0.8 simulation finger patterns have one more finger than the $n = 0.6$ case. In the simulation for $D = 2$, the flattest inclination, the contact lines are completely stable. This is very apparent in the bottom row of Figure 8, and also evident in the LSA results (Figure 1d), where the growth rate is negative for all $D = 2$ simulations. Finally, the 3D simulations in Figure 8 and comparisons to LSA in Table 1 also confirm the results from single-mode simulations and published Newtonian LSA results: as the inclination approaches vertical, the finger wavelengths are smaller, and the growth rate is faster, and this is true for shear-thinning fluids as well.

4. Conclusions

In summary, the LSA results show that the contact line of a gravity-driven spreading front tends to be more unstable on the vertical plane ($D = 0$) than the less-inclined plane ($D = 1$). This trend can be applied for both Newtonian fluids and power-law fluids. We also found that for the same conditions, the growth rate for shear-thinning fluids is smaller than Newtonian fluids. These findings are further verified in our 3D simulation by comparing the growth rate of the finger length for a single-mode perturbation to the growth rate at the same wavelength in the LSA results. Simulations with multiple-mode, randomly imposed perturbations showed how fingers with a typical pattern distance are formed. This typical pattern wavelength is considered relevant to the most unstable growth rate in LSA results according to previous published studies for Newtonian fluids. We carried out a parametric study for different D and n and showed the average distance between finger patterns in our multiple-mode 3D simulations matched the LSA results. We also found that this typical wavelength is the same for both Newtonian and shear-thinning fluids in the vertical case, but it's different in the less-inclined case – the wavelength for a shear-thinning fluid is greater than that for a Newtonian fluid. The multiple-mode 3D simulations also showed the merging of fingers forming atypical patterns commonly observed in actual coating flows and experiments.

Practically, this study can be used in coating flow applications to help avoid the occurrence and/or magnification of the fingering patterns. To improve the coating processes in industrial and biomedical applications, we could optimize the fluid's shear-thinning properties in order to suppress the fingering instability and widen the finger wavelength. Additionally, since the connection between fingering instability and the capillary ridge was obtained here for shear-thinning fluids, the occurrence of the capillary ridge in our previous 2D model can be used for quick assessment of predicted fingering instability at the contact line. Future studies will use this study as a framework to explore more complex contact line physics and rheological models, such as the Ellis' model description of the Newtonian plateau observed at low shear rates in shear-thinning fluids.

Acknowledgments

This work was supported by NIH R21/R33 AI082697 and NIH KI2 HD052027. Some of the computational resources at the KU ITTC high performance computing cluster were funded by NSF MRI 0821625.

References

1. Evans PL, Schwartz LW, Roy RV. A mathematical model for crater defect formation in a drying paint layer. Journal of Colloid and Interface Science. 2000; 227(1):191–205. [PubMed: 10860611]
2. Nong K, Anderson DM. Thin film evolution over a thin porous layer: modeling a tear film on a contact lens. Siam Journal on Applied Mathematics. 2010; 70(7):2771–2795.
3. Pease LF, Russel WB. Electrostatically induced submicron patterning of thin perfect and leaky dielectric films: A generalized linear stability analysis. Journal of Chemical Physics. 2003; 118(8): 3790–3803.
4. Svendsen B, et al. On the role of mechanical interactions in the steady-state gravity flow of a two-constituent mixture down an inclined plane. Proceedings of the Royal Society of London Series a-Mathematical Physical and Engineering Sciences. 1996; 452(1948):1189–1205.

5. Partridge D, Baines MJ. A moving mesh approach to an ice sheet model. Computers & Fluids. 2011; 46(1):381–386.
6. Hu B, Kieweg SL. The effect of surface tension on the gravity-driven thin film flow of Newtonian and power-law fluids. Computers & Fluids. 2012; 64:83–90. [PubMed: 23687391]
7. Szeri AJ, et al. A model of transluminal flow of an anti-HIV microbicide vehicle: Combined elastic squeezing and gravitational sliding. Physics of Fluids. 2008; 20(8)
8. Jossic L, et al. The fluid mechanics of shear-thinning tear substitutes. Journal of Non-Newtonian Fluid Mechanics. 2009; 161(1-3):1–9.
9. Huppert HE. Flow and instability of a viscous current down a slope. Nature. 1982; 300(5891):427–429.
10. Schwartz LW. Viscous flows down an inclined plane - instability and finger formation. Physics of Fluids a-Fluid Dynamics. 1989; 1(3):443–445.
11. Troian SM, et al. Fingering instabilities of driven spreading films. Europhysics Letters. 1989; 10(1):25–30.
12. Bertozzi AL, Brenner MP. Linear stability and transient growth in driven contact lines. Physics of Fluids. 1997; 9(3):530–539.
13. Lin TS, Kondic L. Thin films flowing down inverted substrates: Two dimensional flow. Physics of Fluids. 2010; 22(5)
14. Espin L, Kumar S. Forced spreading of films and droplets of colloidal suspensions. Journal of Fluid Mechanics. 2014; 742:495–519.
15. Espin L, Kumar S. Sagging of Evaporating Droplets of Colloidal Suspensions on Inclined Substrates. Langmuir. 2014; 30(40):11966–11974. [PubMed: 25229746]
16. Gonzalez AG, et al. Spreading of a thin two-dimensional strip of fluid on a vertical plane: Experiments and modeling. Physical Review E. 2004; 70(2)
17. Gomba JM, et al. Stability study of a constant-volume thin film flow. Physical Review E. 2007; 76(4)
18. Balmforth N, Ghadge S, Myers T. Surface tension driven fingering of a viscoplastic film. Journal of Non-Newtonian Fluid Mechanics. 2007; 142(1-3):143–149.
19. Spaid MA, Homsy GM. Stability of Newtonian and viscoelastic dynamic contact lines. Physics of Fluids. 1996; 8(2):460–478.
20. Spaid MA, Homsy GM. Stability of viscoelastic dynamic contact lines: An experimental study. Physics of Fluids. 1997; 9(4):823–832.
21. Kondic L. Instabilities in gravity driven flow of thin fluid films. Siam Review. 2003; 45(1):95–115.
22. Kondic L, Diez J. Flow of thin films on patterned surfaces: Controlling the instability. Physical Review E. 2002; 65(4):4.
23. Kondic L, Diez J. Pattern formation in the flow of thin films down an incline: Constant flux configuration. Physics of Fluids. 2001; 13(11):3168–3184.
24. Kondic L, Diez J. Flow of thin films on patterned surfaces. Colloids and Surfaces a-Physicochemical and Engineering Aspects. 2003; 214(1-3):1–11.
25. Diez JA, Kondic L. Computing three-dimensional thin film flows including contact lines. Journal of Computational Physics. 2002; 183(1):274–306.
26. Lin TS, Kondic L, Filippov A. Thin films flowing down inverted substrates: Three-dimensional flow. Physics of Fluids. 2012; 24(2)
27. Kheyfets VO, Kieweg SL. Experimental and Numerical Models of Three-Dimensional Gravity-Driven Flow of Shear-Thinning Polymer Solutions Used in Vaginal Delivery of Microbicides. Journal of Biomechanical Engineering-Transactions of the Asme. 2013; 135(6)
28. Kheyfets VO, Kieweg SL. Gravity-driven thin film flow of an ellis fluid. Journal of Non-Newtonian Fluid Mechanics. 2013; 202:88–98. [PubMed: 25309029]
29. Macosko, C. Rheology Principles, Measurements, and Applications. 4th edition. Wiley-VCH; New York: 1994.
30. Perazzo CA, Gratton J. Thin film of non-Newtonian fluid on an incline. Physical Review E. 2003; 67(1)

31. Ye Y, Chang HC. A spectral theory for fingering on a prewetted plane. Physics of Fluids. 1999; 11(9):2494–2515.
32. Logg A, Wells GN. DOLFIN: Automated Finite Element Computing. Acm Transactions on Mathematical Software. 2010; 37(2)
33. Logg, A.; Mardal, K-A.; Wells, G. Automated Solution of Differential Equations by the Finite Element Method. Springer; 2012.

Highlights

- Linear stability analysis and 3D simulation of gravity-driven flow of power-law fluid
- Parametric study of power-law index and inclination angle on fingering instability
- More shear-thinning fluids suppress finger growth

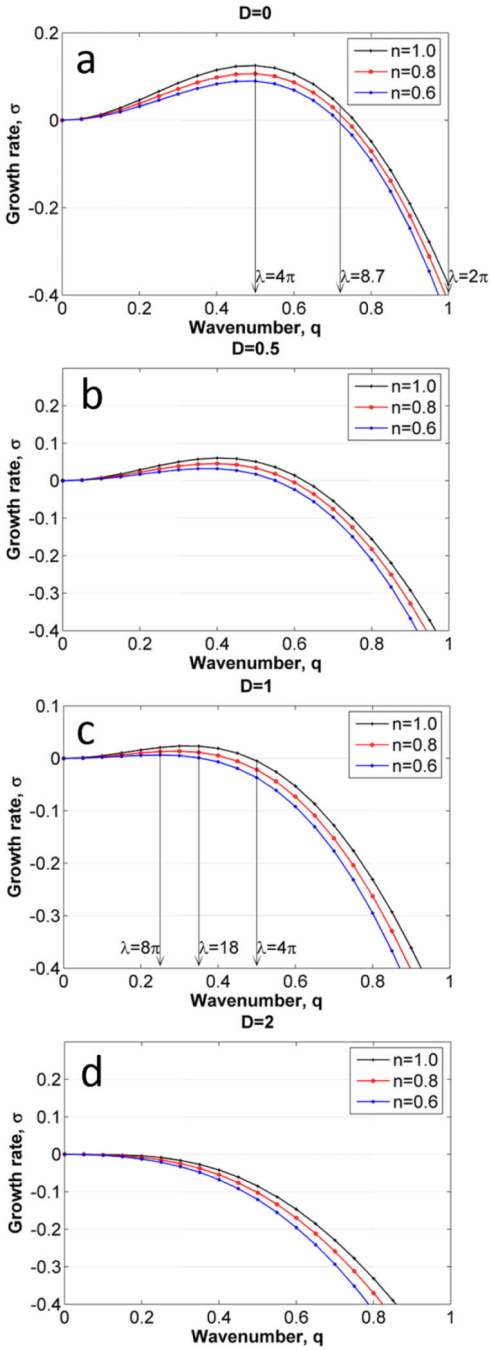

Figure 1. (Color online) The LSA growth rate as a function of wavenumber *q* and power-law index *n*

Comparison among different dimensionless numbers: *D*=0 (a), *D*=0.5 (b), *D*=1 (c) and *D*=2 (d). Figure (b), (d) and the vertical lines in Figure (a) and (b) will be discussed later in Section 3 in conjunction with 3D simulations. (Other simulation parameters: precursor b=0.1, Δx=0.01, Δt=0.01.)

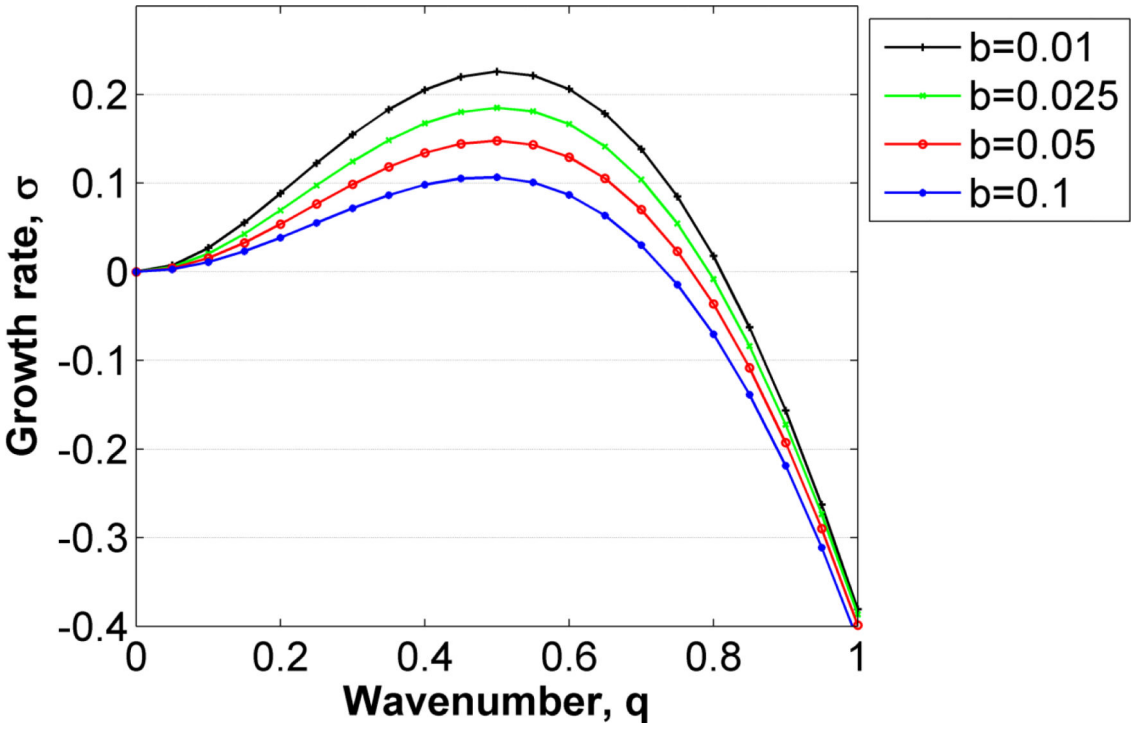

Figure 2. (Color online) Effect of precursor thickness on LSA growth rate for a shear-thinning fluid

b=0.01 (black solid), b=0.025 (green dotted), b=0.05 (red circled), and b=0.1 (blue dotted). (Other simulation parameters: n=0.8, D=0, Δx=0.01, Δt=0.01)

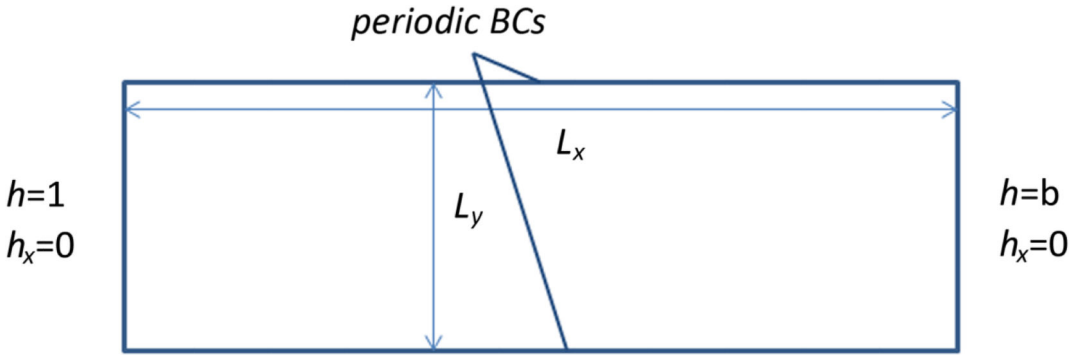

Figure 3. Schematic of the Boundary Conditions (BCs) for the 3D Numerical Simulation

The subscript on h indicates derivative. Flow is in the x-direction downhill to the right, and the domain width is L_y in the y-direction. The constant flux condition is the non-dimensional $h = 1$ at $x = 0$ for all time. The precursor boundary condition is indicated with $h = b << 1$ at the domain boundary $x = L_x$ at all time.

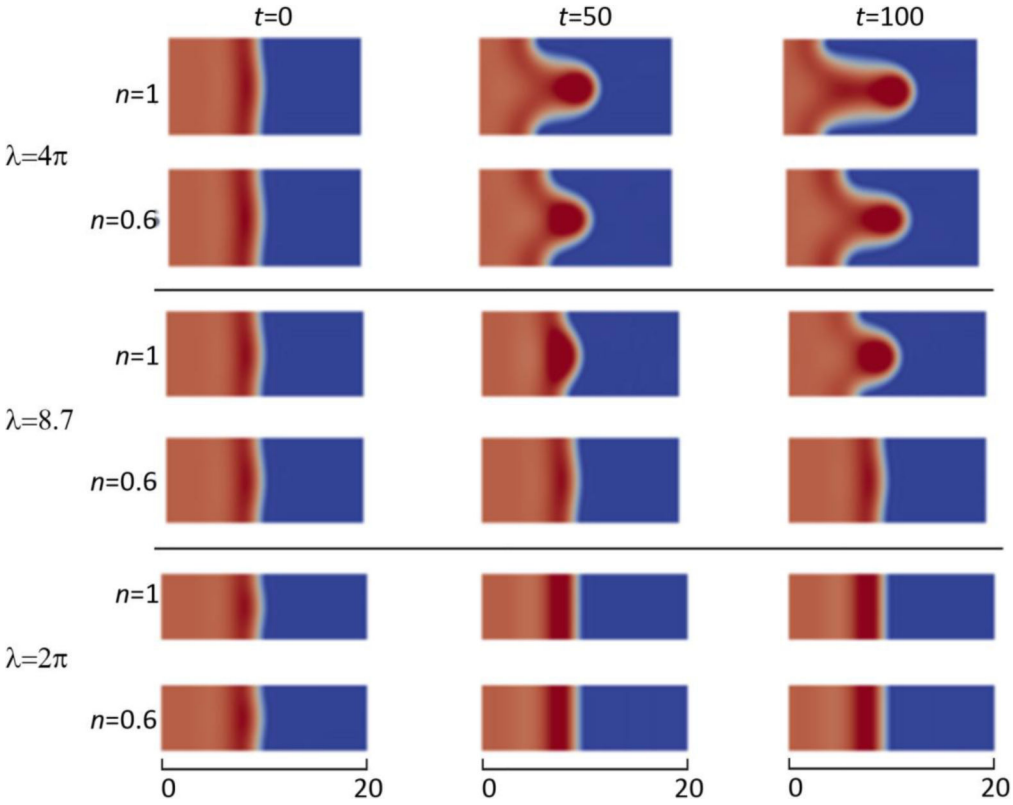

Figure 4. Time series of 3D simulations with single mode perturbation, for $D = 0$

Growth of the fingering patterns for both Newtonian (Row 1, 3, 5) and shear-thinning fluids (Row 2, 4, 6) on a vertical plane ($D = 0$) with perturbations of different wavelengths $\lambda = 4\pi$ 8.7, and 2π. From left to right: $t = 0$, 50, and 100. $L_x = 20$, $L_y = \lambda$ for each simulation.

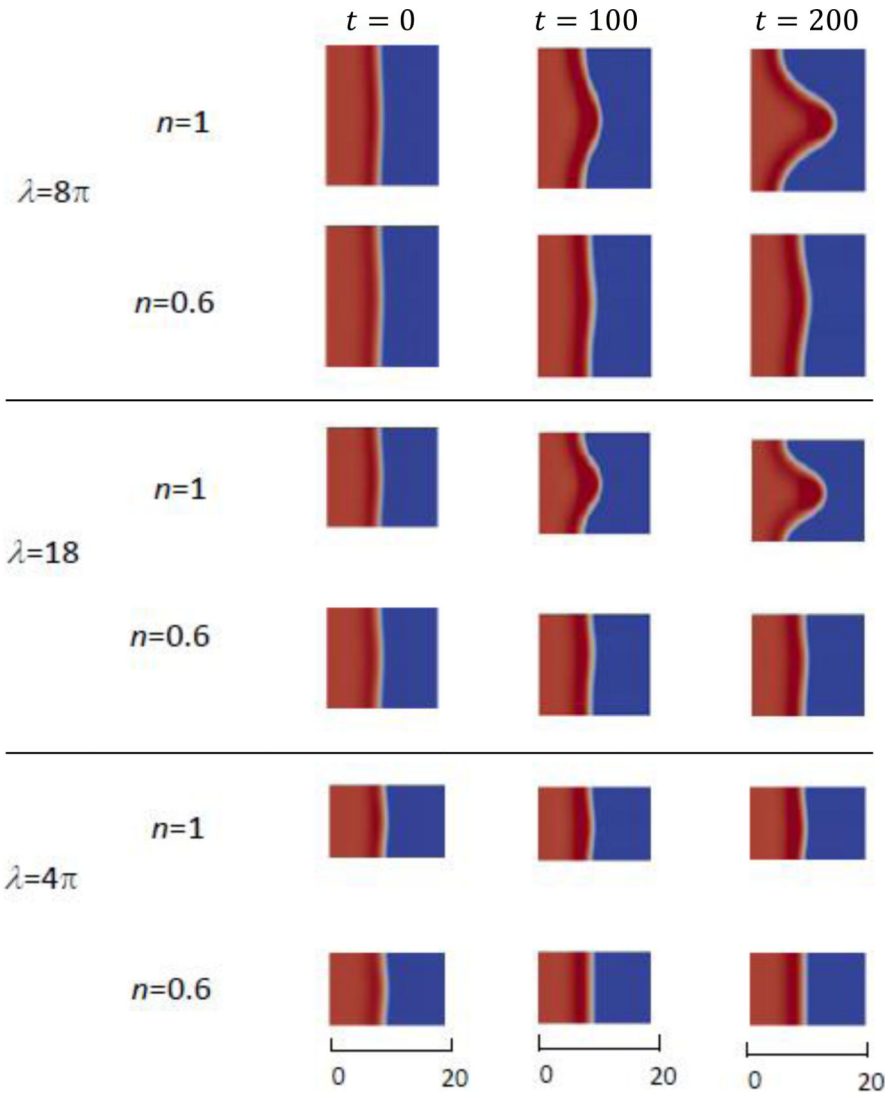

Figure 5. Time series of 3D simulations with single mode perturbation, for $D = 1$

Growth of the fingering patterns for both Newtonian (Row 1, 3, 5) and shear-thinning fluids (Row 2, 4, 6) on a less-inclined plane ($D = 1$) with perturbations of different wavelengths $\lambda = 8\pi$, 18, and 4π. From left to right: t=0, 100, and 200. $L_x = 20$, $L_y = \lambda$ for each simulation.

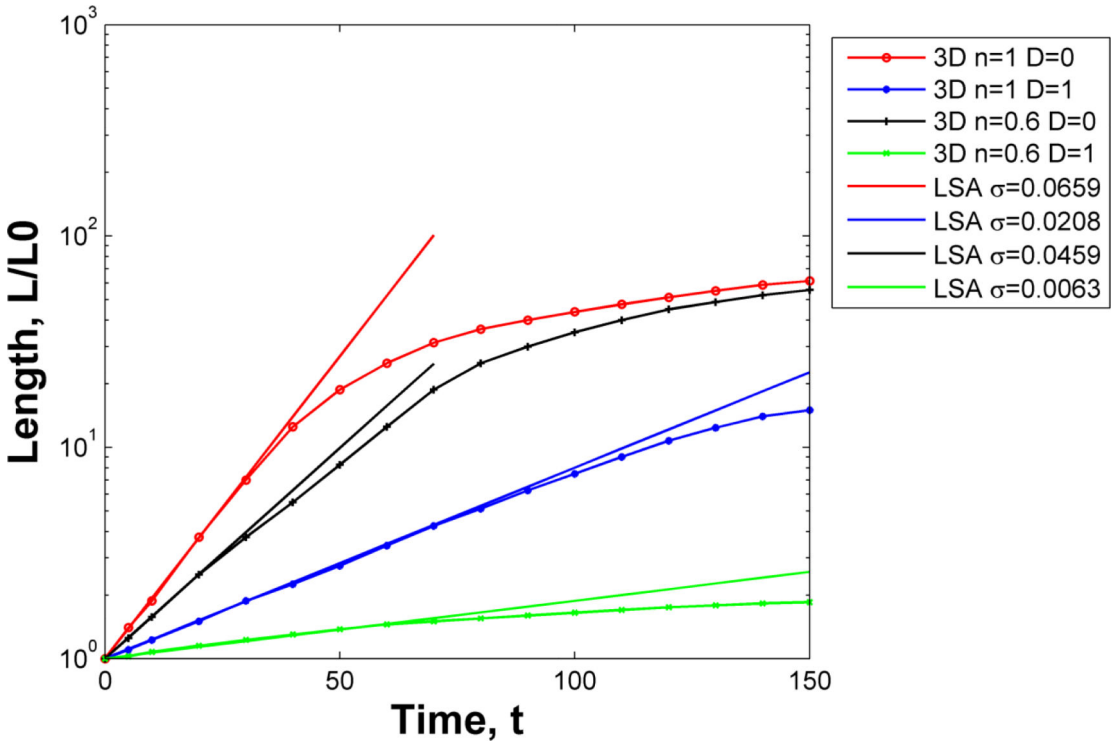

Figure 6. Comparison of growth rates from LSA (solid lines) and single mode 3D simulations (symbols)

The figure shows the finger length (normalized to initial length) vs time for four cases: n = 1, D = 0; n = 1, D = 1; n = 0.6, D = 0; and n = 0.6, D = 1. For each case, the calculated growth from the 3D simulations (symbols) is compared to LSA prediction (solid lines). (All 3D simulations and LSA results used perturbations of wavelength $\lambda = 8\pi$ which provides a positive growth rate for all simulations.)

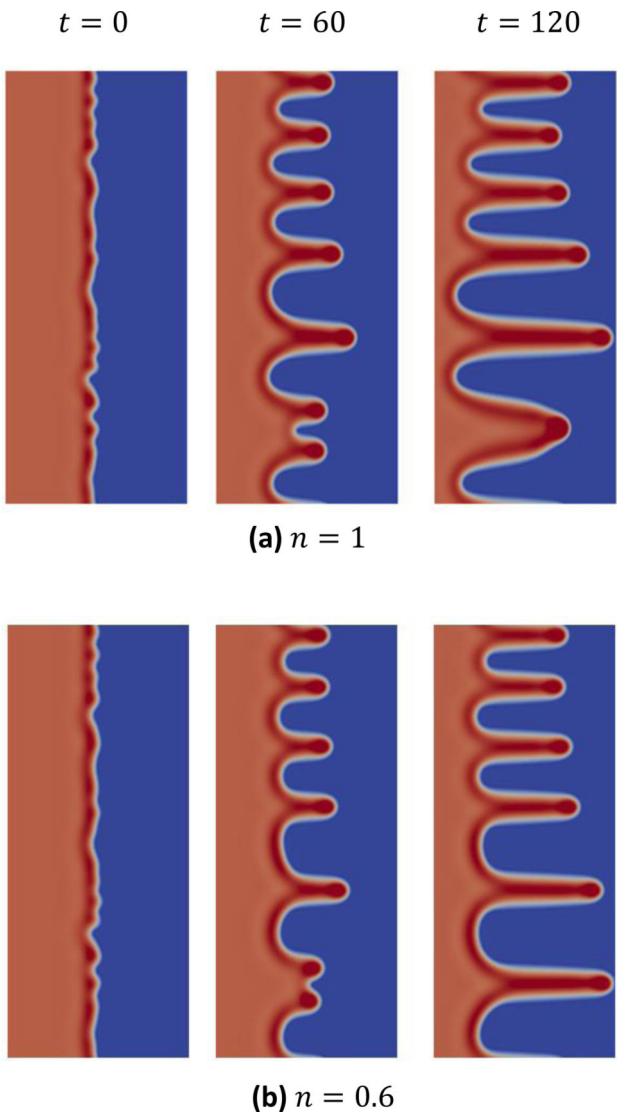

Figure 7. Time-series of 3D simulations with multiple-mode, random perturbations for $D = 0$

Comparison between **(a)** Newtonian $n = 1$ and **(b)** shear-thinning $n = 0.6$ on a vertical plane ($D = 0$, $L_x = 40$, $L_y = 96$). (Left to right, for $t = 0$, 60, and 120.)

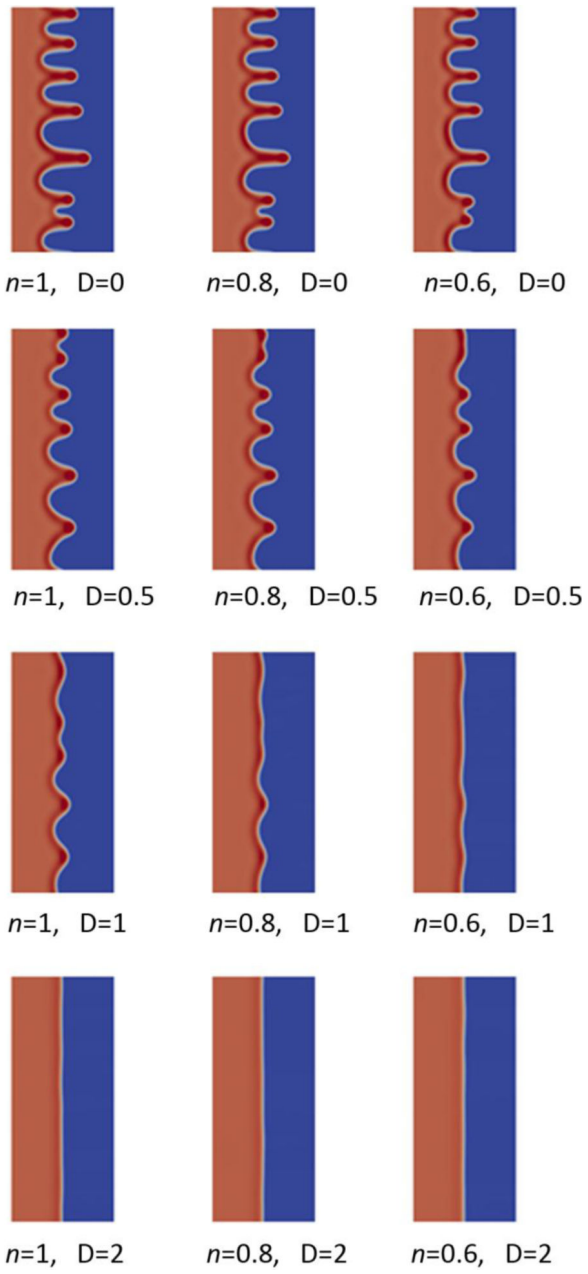

Figure 8. A summary of contact line patterns for 12 simulation cases, each showing only one time point

The points selected were: t = 60, 80, 100 and 120 for D = 0, 0.5, 1 and 2 respectively. These time points are in the regime when the LSA results correspond with the linear portion of the 3D numerical simulations in Figure 6. (L_x = 40, L_y = 96).

Table 1

A summary of comparison between LSA most unstable wavelength (black – top line of each cell) and 3D characteristic wavelength (italic blue – bottom line of each cell)

For the *top line* in each cell, the most unstable wavelength from LSA results (summarized in Fig. 1a-d for four D values)) was calculated as 2π divided by the wavenumber at the maximum growth rate. For the *bottom line* of each cell, the characteristic wavelength of multi-mode simulations was calculated as the simulation width (96) divided by the number of fingers observed in the simulation. For the vertical case, no difference was observed between Newtonian and the most shear-thinning. For the inclined cases with fingering, the most unstable (LSA) and characteristic (3D) wavelength was longest for the most shear-thinning fluid.

D / ***n***	**0**	**0.5**	**1**	**2**
1	$2\pi/0.5=12.566$ *96/7=13.714*	$2\pi/0.4=15.708$ *96/6=16*	$2\pi/0.35=17.950$ *96/5=19.200*	$2\pi/0=\infty$ *No finger*
0.8	$2\pi/0.5=12.566$ *96/7=13.714*	$2\pi/0.4=15.708$ *96/6=16*	$2\pi/0.3=20.944$ *96/5=19.200*	$2\pi/0=\infty$ *No finger*
0.6	$2\pi/0.5=12.566$ *96/7=13.714*	$2\pi/0.35=17.952$ *96/5=19.200*	$2\pi/0.25=25.133$ *96/4=24*	$2\pi/0=\infty$ *No finger*